

© 2022. Guozhu Wang, Xulin Luo, Lei Song, Yu Wang,

Mouwang Han, Zhaocun Song, Linjun Wu, Zukun Wang.

pp. 447–468

This is an open-access article distributed under the terms of the Creative Commons Attribution-NonCommercial-NoDerivatives License (CC BY-NC-ND 4.0, <https://creativecommons.org/licenses/by-nc-nd/4.0/>), which permits use, distribution, and reproduction in any medium, provided that the Article is properly cited, the use is non-commercial, and no modifications or adaptations are made.



Research paper

Analysis of the cracking mechanisms in pre-cracked sandstone under radial compression by moment tensor analysis of acoustic emissions

Guozhu Wang¹, Xulin Luo², Lei Song³, Yu Wang⁴, Mouwang Han⁵,
Zhaocun Song⁶, Linjun Wu⁷, Zukun Wang⁸

Abstract: Rock masses, especially those with different pre-existing cracks, are prone to instability and failure under tensile loading, resulting in different degrees of engineering disasters. Therefore, to better understand the effect of pre-existing cracks with different dip angles on the tensile instability failure behaviour of rocks, the mechanism of crack initiation, propagation and coalescence in pre-cracked sandstone under radial compression loading is investigated through numerical simulations. The temporal and spatial evolution of acoustic emission (AE) events is investigated by the moment tensor (MT), and the fracture mode of micro-cracks is determined. The results show that the pre-existing cracks weaken the specimens. The strength, crack initiation points and macro-failure modes of the specimens differ significantly depending on the dip angle of the pre-existing crack. For different dip angles of the pre-existing cracks, all the micro-cracks at the crack initiation point are tensile cracks, which are dominant during the whole loading process, and mixed cracks are mainly generated near the upper and lower loading ends after the peak stress. Of the total number of events, more than 75% are tensile cracks; approximately 15% are shear mode cracks; and the remainder consist of mixed mode cracks. The study reveals the instability and failure mechanism of pre-cracked rock, which is of great significance to ensure the long-term stability of rock mass engineering.

Keywords: acoustic emission, cracking mechanisms, moment tensor, pre-cracked sandstone, radial compression

¹PhD. St., China University of Mining and Technology (CUMT), State Key Laboratory for Geomechanics and Deep Underground Engineering, Xuzhou 221116, China, e-mail: guozhuwang@cumt.edu.cn, ORCID: 0000-0003-2025-0907

²Prof., PhD., Zhengzhou University of Industrial Technology, School of Architectural Engineering, Zhengzhou 451150, China, e-mail: luoxulin_zuit@163.com, ORCID: 0000-0001-7263-4860

³Prof., PhD., CUMT, Xuzhou 221116, China, e-mail: leisong@cumt.edu.cn, ORCID: 0000-0002-2747-6805

⁴PhD. St., CUMT, Xuzhou 221116, China, e-mail: yuwang@cumt.edu.cn, ORCID: 0000-0003-4538-4055

⁵PhD. St., CUMT, Xuzhou 221116, China, e-mail: 02190803@cumt.edu.cn, ORCID: 0000-0002-0283-3511

⁶PhD. St., CUMT, Xuzhou 221116, China, e-mail: 18260720976@163.com, ORCID: 0000-0003-1905-3754

⁷PhD. St., CUMT, Xuzhou 221116, China, e-mail: TB21220021B1@cumt.edu.cn, ORCID: 0000-0001-7242-2753

⁸PhD. St., CUMT, Xuzhou 221116, China, e-mail: 02180589@cumt.edu.cn, ORCID: 0000-0003-3975-2413

1. Introduction

Rock is a natural brittle material, its tensile strength is far less than its compressive strength, and tensile failure is one of the main forms of rock instability failure in engineering [1–5]. In particular, due to the existence of initial cracks with different shapes, sizes and geometric distributions, the tensile failure behaviour of this kind of rock mass is usually complex [6–9]. The initial cracks will not only reduce the strength of the rock mass but also induce new cracks [10–12]. Therefore, an in-depth understanding of the tensile characteristics of pre-cracked rock masses is of great significance to ensure the long-term stability of rock mass engineering.

To understand the tensile properties of pre-cracked rock, researchers have conducted a large number of experimental studies with rich results. In the 1970s and 1980s, Awaji and Sato [13] and Atkinson et al. [14] conducted a series of experimental studies on the pre-cracked Brazilian disc to study the stress intensity factors. It was found that the stress intensity factors depends on the length and dip angle of the pre-existing crack. During the research process, the type I and type II fracture toughness values were determined. Luo et al. [15] conducted a series of radial compression tests on pre-cracked Brazilian discs with different dip angles and lengths to study the effects of pre-cracks on the mechanical properties, crack initiation and propagation of Brazilian discs. Zhou et al. [16] conducted Brazilian tests at different loading angles on the filling of a central straight notched Brazilian disc to study the effect of filling cracks on crack propagation. Erarslan and Williams [17] conducted static and cyclic radial compression tests on an inclined cracked chevron notched Brazilian disc and found that the dip angles of pre-existing cracks and loading conditions have a strong impact on the opening and closing of cracks, crack initiation point and angle.

At present, research regarding the macro law of pre-existing cracks on rock tensile properties has been quite sufficient. However, the microscopic characteristics of crack initiation and propagation in the rock tensile process are difficult to obtain through laboratory tests. Therefore, numerical simulation has been widely used in the study of the micro-failure mechanism of pre-cracked rock because of its fast and convenient advantages [18–21]. Among them, the discrete element method has significant advantages in analysing the micro-failure mechanism of rock masses [22–24]. Hazzard and Young [25] introduced MT theory into the PFC numerical model and developed a MT model of AE, which provides a new perspective for analysing the micro-mechanisms of rock mass fractures. The simulation of AE events can not only provide a deep understanding of the micro-fracture mechanism of pre-cracked rock masses but also lay a solid foundation for the study of the fracture micro-seismic activity of fractured rock masses.

As commonly accepted, the macro failure of rock is formed by the propagation and coalescence of micro-fractures. Therefore, to deeply understand the micro mechanism of crack initiation and propagation of pre-cracked rock mass under tensile loading, a series of laboratory tests were carried out on pre-cracked sandstone disc samples with different dip angles. Then, the numerical model is verified by the macro failure mode and stress–strain curve obtained from the test. Finally, the numerical simulation is carried out by using the

verified numerical model. The MT of an AE event is decomposed into a spherical tensor and a partial tensor to study the temporal and spatial evolution of AE events and determine the failure form of micro-cracks and focal parameters such as moment magnitude.

2. Modelling method

In this paper, particle flow software for the discrete element method, and an AE MT algorithm [25] are used to simulate the failure mechanism of pre-existing cracks in red sandstone under radial compression loading.

2.1. Selection of the bonding model

The selection of the bond model is central to discrete element calculations. The parallel bond model (as shown in Fig. 1) in particle flow code (PFC) numerical software is used to simulate adhesive materials between particles that are in contact [18, 26]. The parallel bond model can be regarded as a spring with normal and tangential components of bond stiffness on the contact surface, and these components can be transferred to both force and moment. As shown in Fig. 1, [A] and [B] represent two particles that are in contact; $x_i^{[A]}$, $x_i^{[B]}$ and $x_i^{[C]}$ denote the centre coordinates of particles [A], [B] and bond respectively; \bar{R} is the bond radius, and \bar{L} is the bond thickness. The initial values of the force \bar{F}_i and moment \bar{M}_i are zero after parallel bonding. \bar{F}_i and \bar{M}_i can be decomposed into normal components \bar{F}_i^n and \bar{M}_i^n , and tangential components \bar{F}_i^s and \bar{M}_i^s , respectively. Under the

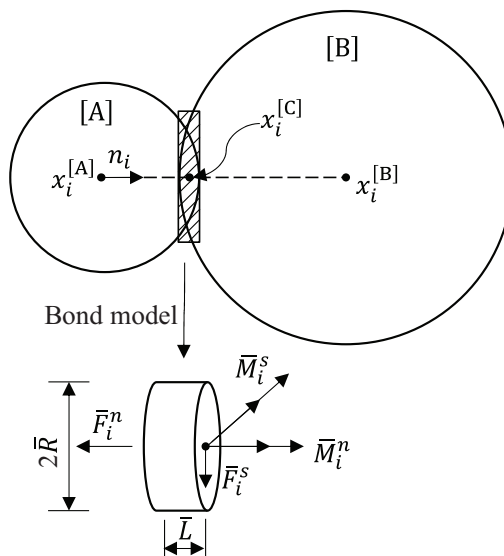


Fig. 1. Parallel bond model

action of an applied load, the normal stress $\bar{\sigma}$ and the tangential stress $\bar{\tau}$ on the parallel bond can be expressed as:

$$(2.1) \quad \begin{cases} \bar{\sigma} = \frac{-\bar{F}^n}{A} + \frac{|M_i^s| \bar{R}}{I} \\ \bar{\tau} = \frac{|F_i^s|}{A} + \frac{|M_i^n| \bar{R}}{J} \end{cases}$$

where, A is the area of the parallel bonding interface, J is the polar moment of inertia of the interface, and I is the moment of inertia of the interface along the contact point in the direction of rotation. Similarly, when the normal or tangential stress exceeds the corresponding parallel bond strength $\bar{\sigma}$ or $\bar{\tau}$, parallel bond failure occurs, resulting in tensile micro-cracks or shear micro-cracks, respectively.

According to the existing numerical simulation studies, the parallel bond model has been widely used in sandstone simulations [27–29]. Therefore, the parallel bond model was chosen in this study.

2.2. AE simulation method and MT decomposition

It is well known that the rupture strengths of earthquakes, microseisms and AEs generally follow exponential distributions. In the process of a PFC micro-fracture simulation, if each micro-fracture is regarded as an AE event and the rupture strength is calculated according to the source information for micro-fracture inversion, then the rupture strength is almost the same for all AE events, which is seriously inconsistent with the distribution law of rupture strengths observed in laboratory tests and field monitoring. Therefore, when the PFC code is used to simulate an AE, it is assumed that multiple micro-cracks are generated by bond fracture. If micro-cracks are relatively close in time and space, then they are considered to be the same AE event.

When the discrete element method is used for a numerical calculation, the MT is the displacement caused by the force acting on the particle surface, which can be equivalent to the effect of physical force. With the movement of the source particles, their bonding states change after a bond failure, which leads to a changes in the contact force. The loaded area of a micro-crack is the area defined by the centre of the micro-crack and a radius equal to the largest diameter of the source particles. Therefore, by multiplying the changes in all the contact forces on the source particle by the corresponding force arms (the distance between the contact point and the centre of the micro-crack), the MT component can be obtained by the summation operation as [25]:

$$(2.2) \quad M_{ij} = \sum_s (\Delta F_i R_j)$$

where: ΔF_i is the i th component of the contact force variation, and R_j is the j -th component of the distance between the contact point and the micro-crack centre. If the AE event contains only one micro-crack, the spatial location of the AE event is the centre of the

micro-crack. If the AE event consists of multiple micro-cracks, the geometric centre of all micro-cracks is the spatial location of the AE event.

The energy released by AE events evolves with time, so the MT can be expressed as a function of time. To save compute costs and improve the compute efficiency, the MT with the maximum scalar moment is used to characterise each AE event. The expression of the scalar moment is

$$(2.3) \quad M_0 = \left(\sum_{j=1}^3 m_j^2 / 2 \right)^{1/2}$$

where m_j is the j -th eigenvalue of the MT matrix.

Furthermore, according to the peak scalar moment of an AE event MT, the calculated AE event rupture strength is

$$(2.4) \quad M = \frac{2}{3} \lg M_0 - 6$$

If the MT calculated by formula (2.2) is decomposed into a spherical tensor and a partial tensor, then the AE rupture type can be evaluated according to the proportion of the spherical tensor [30].

$$(2.5) \quad \begin{cases} P_{\text{ISO}} \geq 30\% & \text{Tensile crack} \\ -30\% < P_{\text{ISO}} < 30\% & \text{Shear crack} \\ P_{\text{ISO}} \leq -30\% & \text{Mixed-mode crack} \end{cases}$$

2.3. Construction of the numerical model

Sandstone is one of the most common geological rock masses in underground engineering rock mass [31]. The rock sample used in this study is red sandstone, with a reddish brown appearance, massive fine-grained sandy structure, pore cementation, and no visible cracks observed by naked eyes. In order to reduce the adverse effect of material heterogeneity, the rock samples used are taken from the same rock. The mineral contents are quartz, potash feldspar, plagioclase, calcite, clay minerals and a small amount of haematite. The size of the red sandstone disk sample is $\Phi 50 \text{ mm} \times 25 \text{ mm}$, and a small drilling rig and emery rope saw [32, 33] are used to prefabricate a crack with a length of $2a = 15 \text{ mm}$ and a width of 0.8 mm in the centre of the disc. At the same time, a cylinder specimen with dimensions $\Phi 50 \text{ mm} \times H 100 \text{ mm}$ is made for the uniaxial compression test. The test was carried out on a DNS 300 rock servo-controlled testing machine at the China University of Mining and Technology, and the loading test was carried out by the displacement control method with a loading rate of 0.01 mm/s . The physical and mechanical parameters of the red sandstone obtained from the test are shown in Table 1. The size of the PFC numerical simulation sample is consistent with that of the sample used in the laboratory loading tests. To comprehensively study the influence of the loading angle on the fracture behaviour of pre-cracked discs, seven pre-existing crack dip angles are used in this paper

($\beta = 0^\circ, 15^\circ, 30^\circ, 45^\circ, 60^\circ, 75^\circ$ and 90°), as shown in Fig. 2. To simulate the laboratory loading test more realistically and effectively, displacement-controlled loading is also used in the simulation; that is, simulated loading is carried out by moving the upper and lower walls, and the loading rate is 0.05 m/s.

Table 1. Physical and mechanical properties of red sandstone

ρ (kg/m ³)	V_P (km/s)	σ_c (MPa)	σ_t (MPa)	E (GPa)	ν	φ (%)
2434.73	2.9465	76.56	6.52	16.47	0.21	9.71

P – density; V_P – P-wave velocity; σ_c – compressive strength; σ_t – tensile strength; E – Young’s modulus; ν – Poisson’s ratio; φ – porosity

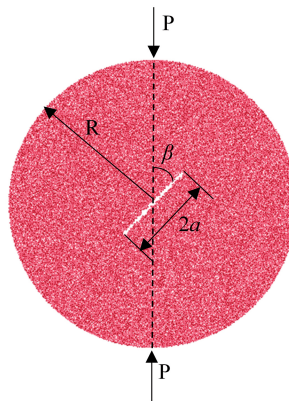


Fig. 2. Numerical model of a pre-cracked disc

2.4. Micro-parameters calibration

Before the particle flow simulation of the loading test, the micro-parameters should be calibrated reasonably. The parallel bond model mainly includes the particle contact modulus, parallel bond modulus, parallel bond stiffness ratio, friction coefficient, parallel bond strength and other micro-parameters. After selecting the relevant micro-parameters, a numerical simulation was carried out to obtain the stress–strain curve, failure mode and other results; these simulation results were compared with the corresponding macro-mechanical parameters obtained from the laboratory test. The “trial and error method” was used for continuous debugging until the simulation results were close to those from the laboratory test. The final micro-parameters selected for the numerical model are shown in Table 2.

To show the rationality of the micro-parameters in Table 2, the failure mode and stress–strain curve obtained by the numerical simulation are compared with the results obtained by the test, as shown in Fig. 3. According to Fig. 3, the failure modes obtained by numerical

Table 2. Micro-parameters for red sandstone

Parameters	Value	Parameters	Value
Minimum particle size (mm)	0.15	Friction coefficient	0.5
Maximum particle size (mm)	0.24	Parallel bond tensile strength (MPa)	26.5
Density ($\text{kg}\cdot\text{m}^{-3}$)	2400	Parallel bond cohesion (MPa)	32
Porosity	0.15	Parallel bond friction angle ($^{\circ}$)	45
Contact bond modulus (GPa)	0.6	Parallel bond modulus (GPa)	7.0
Contact bond stiffness ratio	1.0	Parallel bond stiffness ratio	1.5

simulation and testing are tensile splitting failure. The tensile strength measured by the intact disk test is 6.52 MPa, while the tensile strength calculated by numerical simulation is 6.61 MPa, with a difference of only 1.4%. Because at least three particles are in contact with a given particle in PFC, the particles are relatively close together, which makes it impossible to simulated the initial pore compression stage of the sample, so the peak strain in the numerical simulation is less than in the test.

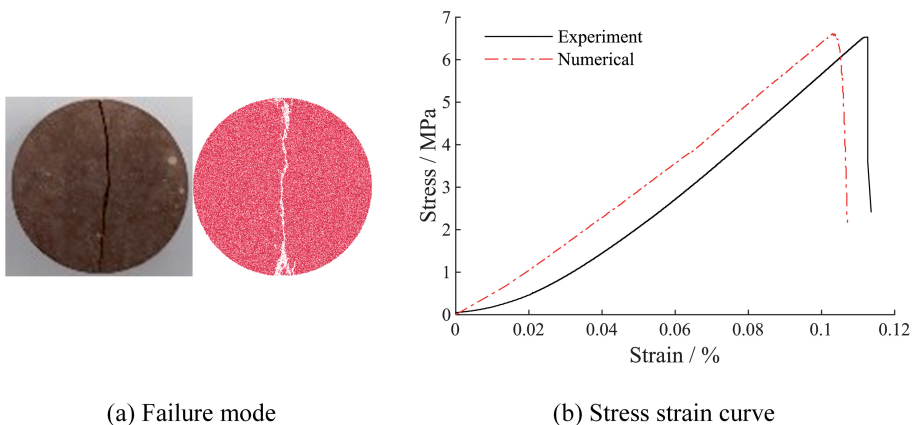


Fig. 3. Comparison of numerical simulation results and experimental results

Comparing the results of the radial compression test and PFC simulation shows that, the micro-parameters selected in this paper are reasonable. The results show that the PFC simulation results are very close to the laboratory test results, which verifies the rationality of the micro-parameters. The comparison of stress–strain and failure modes under different pre-existing crack dip angles is shown in Table 3.

Figure 4 shows the variation in the average value of the tensile strength of pre-cracked sandstone with pre-existing crack dip angle β in the laboratory tests and particle flow simulations. Fig. 4 shows that in the laboratory tests, the tensile strength of the pre-cracked disc is significantly lower than that of the intact disc, and the tensile strength has a nonlinear relationship with the dip angle β , first decreasing, then increasing, then decreasing again,

Table 3. Comparison of the numerical simulation and experimental results

Dip angle	Stress–strain curve	Test results	Numerical results
0°			
15°			
30°			
45°			
60°			
75°			
90°			

and finally increasing once more. The results show that the tensile strength of rock specimen modelling in PFC^{2D} is consistent with that of the laboratory test, but the tensile strength of rock specimen modelling in PFC^{2D} is larger than that of the laboratory test for the same dip angle β , because the specimen composed of a two-dimensional disk in PFC^{2D} cannot fully simulate complex three-dimensional heterogeneous sandstone. The above analysis shows that the selected micro-parameters can better study and simulate the mechanical parameters of sandstone under loading.

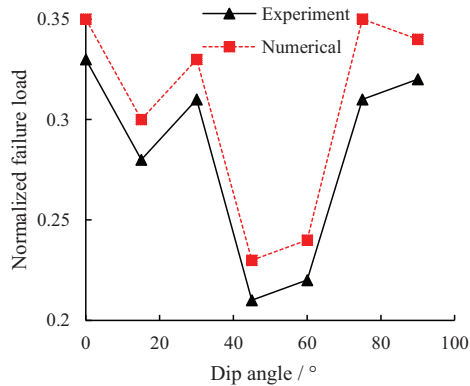


Fig. 4. Normalized failure load versus dip angle of the crack

3. Results and interpretation

3.1. Micro-crack distribution

Due to the influence of cracks on AE signal propagation, most of the current experimental studies mainly focus on AE-MT information before the peak stress [34, 35]. However, many practical results show that crack propagation in the post-peak stage is very important for the fracture of rock masses. Therefore, in this paper, the AE-MT numerical algorithm is used to study the distribution characteristics and fracture mechanism of micro-cracks in pre-peak and post-peak stages of pre-cracked red sandstone disks. Because discrete element software cannot truly express the pre-peak pore compaction stage, the crack space evolution process of 90% before the peak, the peak, 95% after the peak, 90% after the peak and 85% after the peak (90%, 100%, 105%, 110% and 115% below) is mainly studied.

Figs. 5–11 show the spatial distribution of different types of cracks under radial compression. The blue circles represent tensile cracks, the red rectangles represent shear cracks, and the green triangles represent mixed cracks.

When the pre-existing crack dip angle is $\beta = 0^\circ$ (Fig. 5), the damage inside the sample is small before the peak stress; only a small number of micro-cracks are found at the upper and lower loading ends and the pre-existing crack tip, and these is a small number of tensile cracks, which indicates that the tensile stress begins to concentrate in the pre-existing

crack tip area. When the stress reaches the peak stress, the micro-cracks grow rapidly from the pre-existing crack tip to the loading end, and the specimen is mainly subject to axial splitting failure, which is caused by two tensile cracks at both ends of the pre-existing crack. During this period, tensile mode cracks are dominant, accompanied by a small number of shear mode cracks; and the mixed mode cracks are mainly generated at the upper and lower loading ends, which is consistent with the macro-fracture results in Fig. 5f.

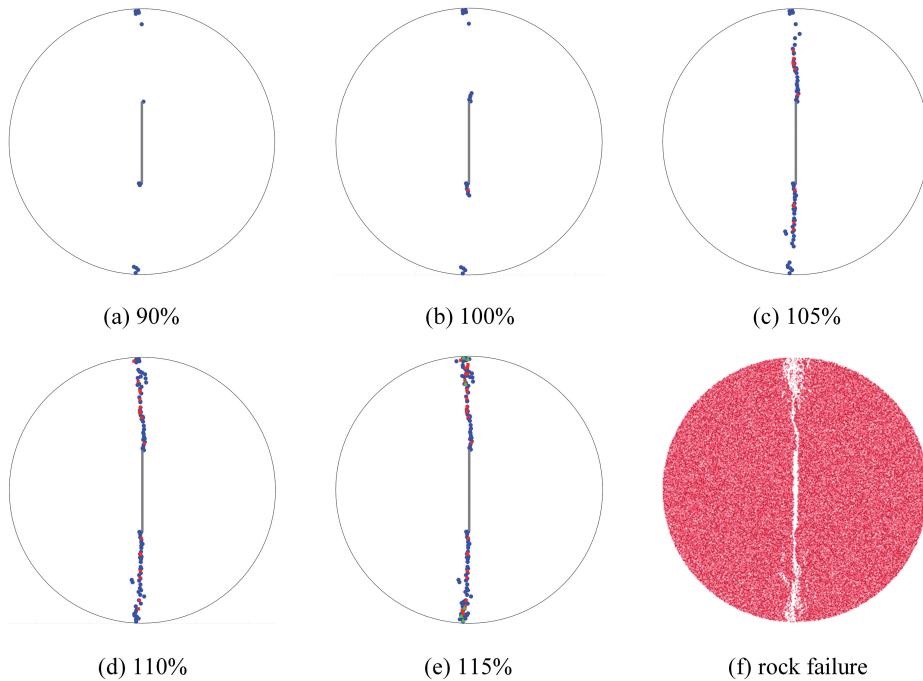


Fig. 5. Spatial distribution of different types of cracks with stress ($\beta = 0^\circ$)

When the angle of pre-existing crack is $\beta = 15^\circ$ (Fig. 6), the position of the crack initiation point and the process of micro-crack propagation are similar to those when the angle of pre-existing crack is 0° . However, when the pre-existing crack angle is 15° , the growth rate of the upper crack is not faster than that of the lower crack, and tensile micro-crack are dominant throughout the loading process. This different from the pre-existing crack dip angle is 0° , because mixed mode cracks begin to appear after the peak stress at the pre-existing crack dip angle is 15° .

It can be seen from Fig. 7 to Fig. 9 that the macro-failure mode of the specimen is shear failure, which is different from macro-failure when the pre-existing crack dip angle is 0° and 15° in that micro-cracking is always accompanied by shear micro-cracking during the whole propagation process. Although tensile micro-cracks always dominate, shear micro-cracks are distributed uniformly during loading. This is mainly because the radial region of the disk is mainly affected by the tensile stress under radial compression loading. Moreover,

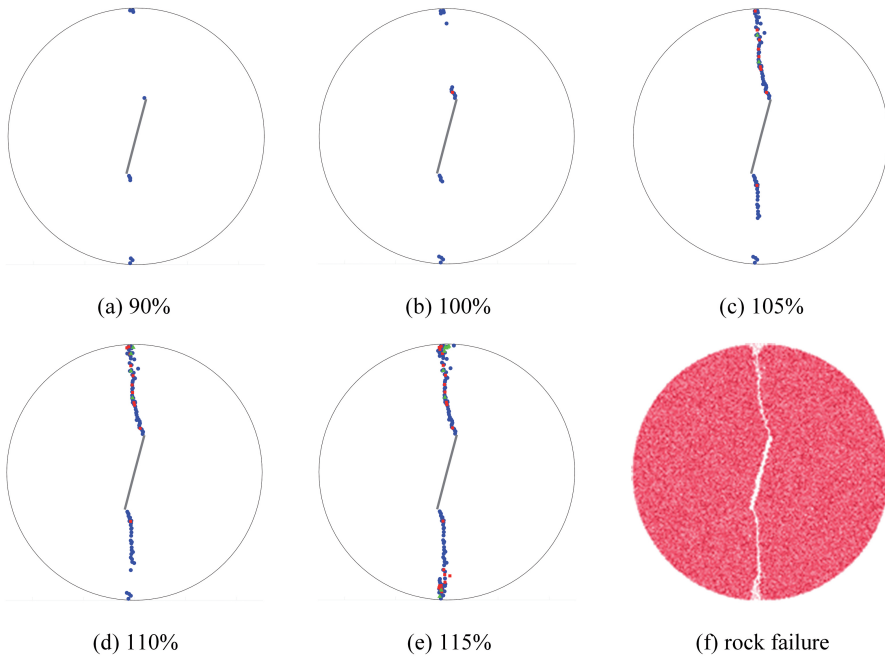


Fig. 6. Spatial distribution of different types of cracks with stress ($\beta = 15^\circ$)

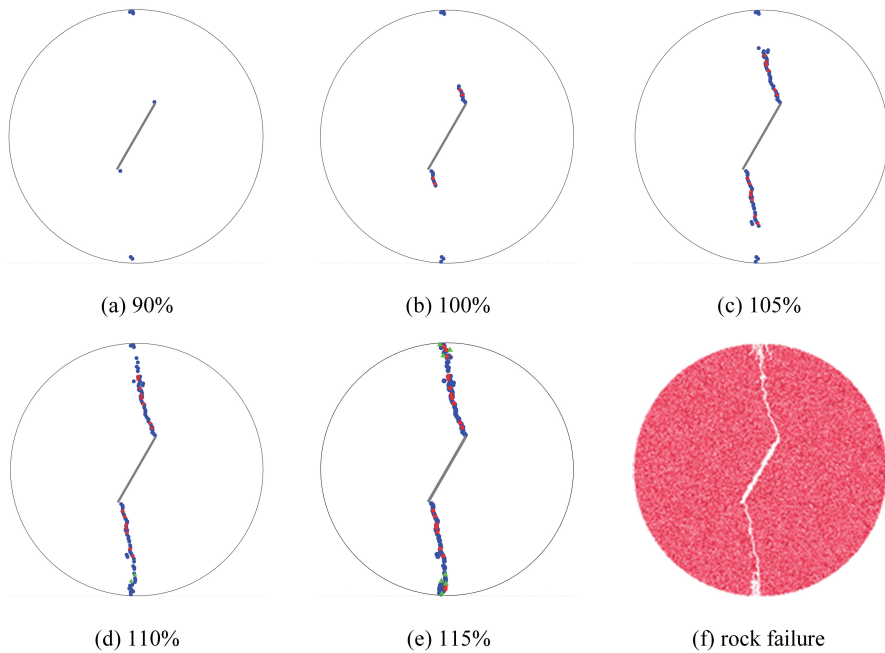


Fig. 7. Spatial distribution of different types of cracks with stress ($\beta = 30^\circ$)

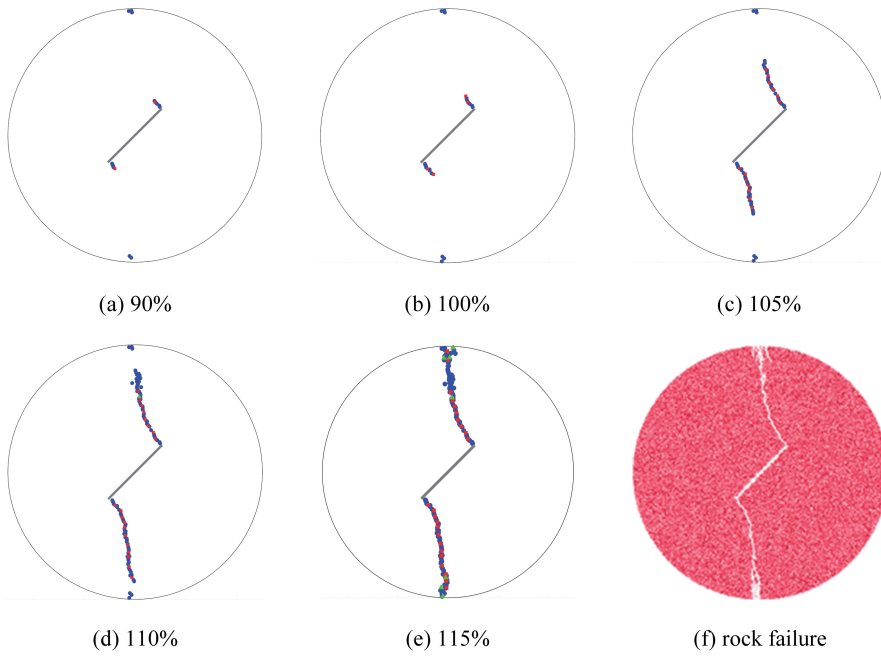


Fig. 8. Spatial distribution of different types of cracks with stress ($\beta = 45^\circ$)

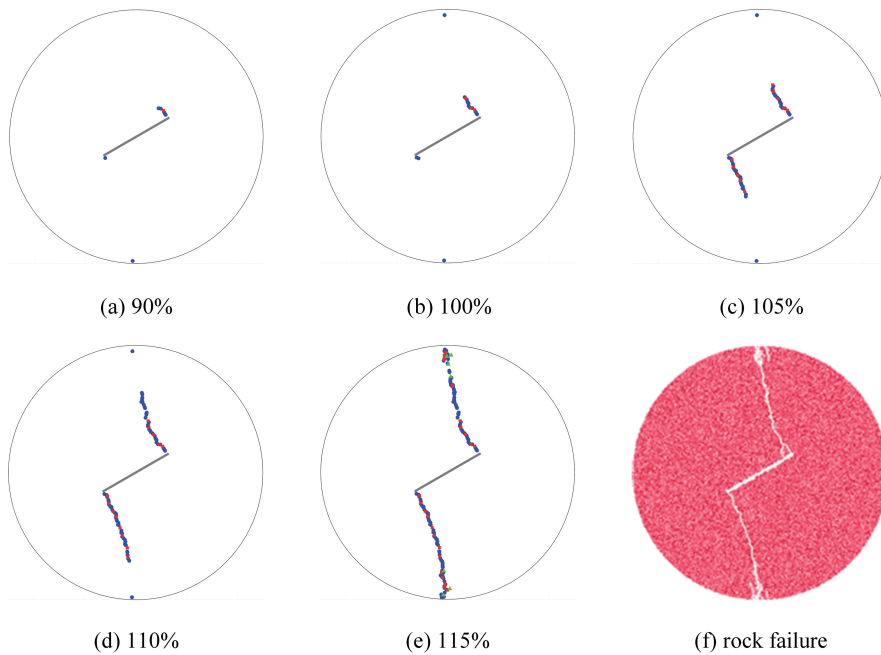


Fig. 9. Spatial distribution of different types of cracks with stress ($\beta = 60^\circ$)

the micro-mechanism of crack failure is very different from the macro-mechanism, and the sizes of the micro-cracks are mainly in the mm range.

It can be seen from Fig. 10 and Fig. 11 that with the increase in the dip angle of the pre-existing crack, the crack does not start from the tip of the pre-existing crack, but at a certain distance from the tip of the pre-existing crack, and the crack initiation times of the upper and lower cracks are also different. When the angle of the pre-existing crack is 90° , the crack initiation point is basically at the centre of the disc.

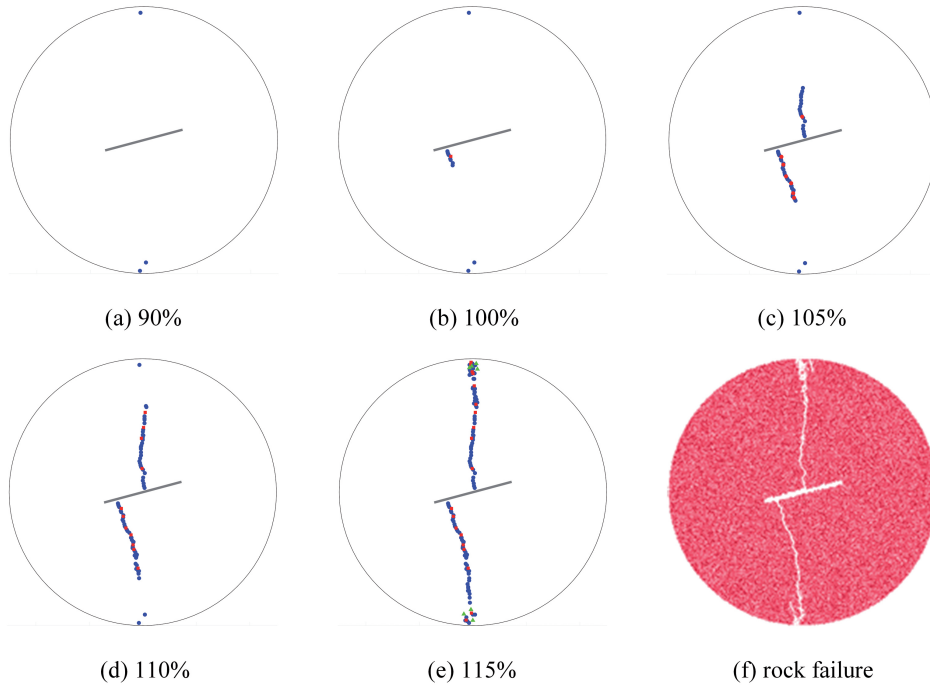


Fig. 10. Spatial distribution of different types of cracks with stress ($\beta = 75^\circ$)

Fig. 5 to Fig. 11 show that the angle of the pre-existing crack has different effects on the macro- mechanical and micro-mechanical mechanisms, such as the crack initiation point, crack propagation process and micro-crack distribution. However, the common points are as follows: (1) regardless of the location of the crack initiation point, the micro-crack at the crack initiation point is always a tensile crack, which is mainly due to the influence of the loading mode and tensile stress concentration at the crack tip. The existing numerical analysis results show that there is a large tensile stress concentration at the crack tip, which is the fundamental reason for crack initiation and propagation. (2) In the process of micro-crack propagation, tensile cracks are always dominant, primarily because the radial region of the disk is mainly affected by the tensile stress under radial compression loading, and the shear stress cannot be concentrated in a certain region during the loading process, forming a larger shear stress concentration region. (3) Mixed mode cracking mainly occurs

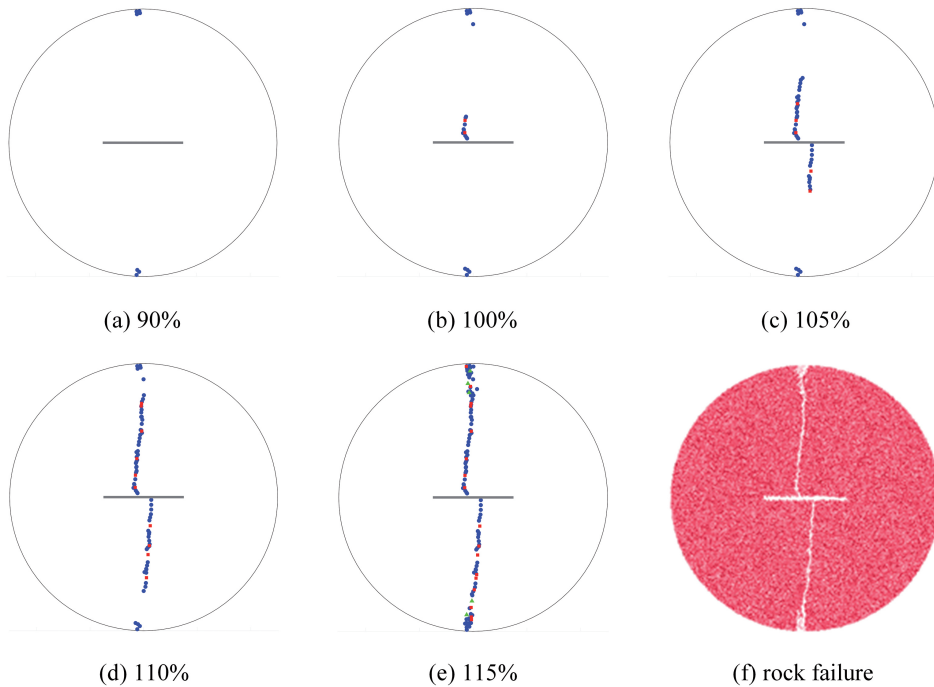


Fig. 11. Spatial distribution of different types of cracks with stress ($\beta = 90^\circ$)

after the peak stress, primarily because mixed mode cracking has an internal contraction component, and the internal contraction mechanism occurs only when the macro-crack reaches a certain degree.

3.2. Percentage of tensile cracks, shear cracks and mixed mode cracks

Figure 12 shows that tensile cracks are dominant during the whole loading process of specimens with different pre-existing crack dip angles. Before the peak stress, there are few shear cracks and no mixed cracks. Many micro-cracks occur after the peak stress. Table 4 shows that approximately 80% of the AE events are caused by tensile fracture, approximately 15% are caused by shear fracture, and only approximately 5% are caused by mixed fracture. The AE events of tensile fracture are much larger than those of shear fracture and mixed fracture, which indicates that the AE events are mainly caused by tensile failure in the specimen under radial compression loading, and only a few AE events are caused by shear failure or mixed failure, which is basically consistent with the previous research results. There is no fixed proportion of the crack types that produce AE in the process of loading to failure, and the proportion of each crack type is related to the loading conditions and internal structure of the sample.

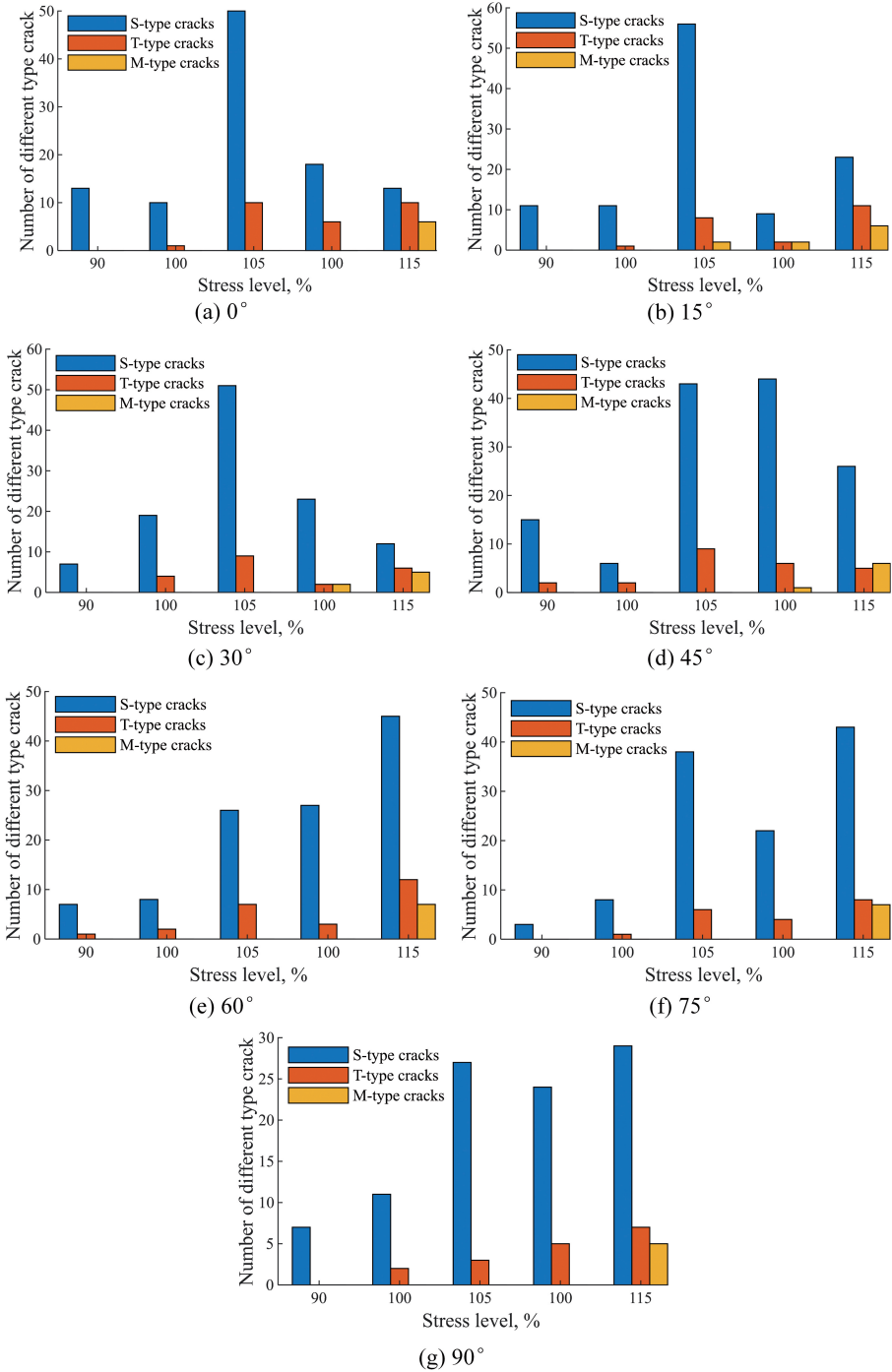


Fig. 12. Fracture types under different stress levels

Table 4. Ratios of fracture types of AE events

Dip angle (°)	Total number of cracks	Tensile fracture (%)	Shear fracture (%)	Mixed fracture (%)
0°	137	75.91	19.71	4.38
15°	142	77.46	15.50	7.04
30°	140	80.00	15.00	5.00
45°	165	81.21	14.55	4.24
60°	145	77.93	17.24	4.83
75°	140	81.43	13.57	5.00
90°	120	81.66	14.17	4.17

3.3. Magnitude analysis of AE events

In seismology, the b value represents the relationship between the earthquake magnitude and frequency, i.e., the Gutenberg–Richter relation [36]:

$$(3.1) \quad \log N = a - bM$$

where M is the magnitude of earthquakes; N is the number of earthquakes in the range of $M + \Delta M$; a is the constant of seismicity degree; and b is the b value in seismology, which is only for the magnitude range on the right side of the peak magnitude in the magnitude frequency distribution. Therefore, the b value is equal to the absolute value of the slope of the regression line between M and $\log N$ in a certain range on the right side of the peak magnitude.

Figure 13 shows the relationship between the AE event frequency and AE magnitude of samples with different pre-existing crack dip angles. The AE magnitudes of all samples are between -8.5 and -7.0 , and the b values are between 1.52 and 2.00. The results of Kim et al. [37] show that the b values of sandstone are between 1.5 and 2.5, which also shows the correctness of the AE-MT programme used in this paper. The conditions of pre-existing crack dip angles of 75° and 90° are excepted, when the magnitude is greater than -8.0 , the cumulative number of AEs increases rapidly with decreasing magnitude. It should be noted that the distribution range of high-frequency magnitudes of specimens with pre-existing crack dip angles of 45° and 60° is relatively narrow. According to Fig. 4, when the dip angles are 45° and 60° , the bearing capacity of the specimens is relatively low, and the specimens are most likely to be damaged during the loading process, which is consistent with the research results of Ghazvinian et al. [38].

The relationship between the number of AE events and the number of micro-cracks in each AE event is shown in Fig. 14. The results show that the relationship between the number of AE events and the number of micro-fractures approximates negative exponential function. The number of AE events with only one micro-fracture is the highest, accounting for approximately 50–60% of the total number of AE events. If more than one micro-cracks is produced in each AE event, then the number of AE events decreases rapidly

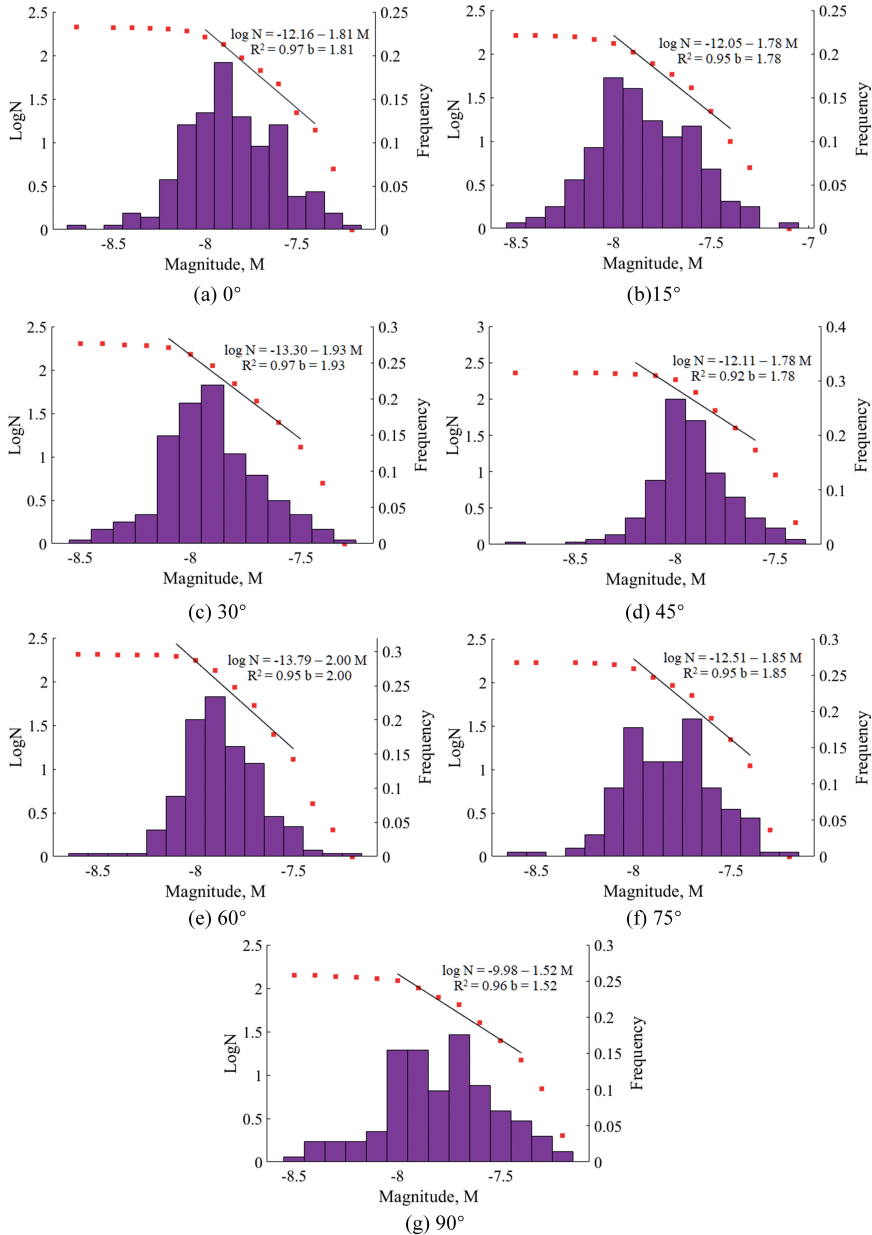


Fig. 13. Relationship between AE event frequency and AE magnitude

with increasing number of micro-cracks. Approximately 20% of AE events contain two micro-fractures. The number of AE events with 10 or more micro-fractures accounts for only 1% of the total number of AE events.

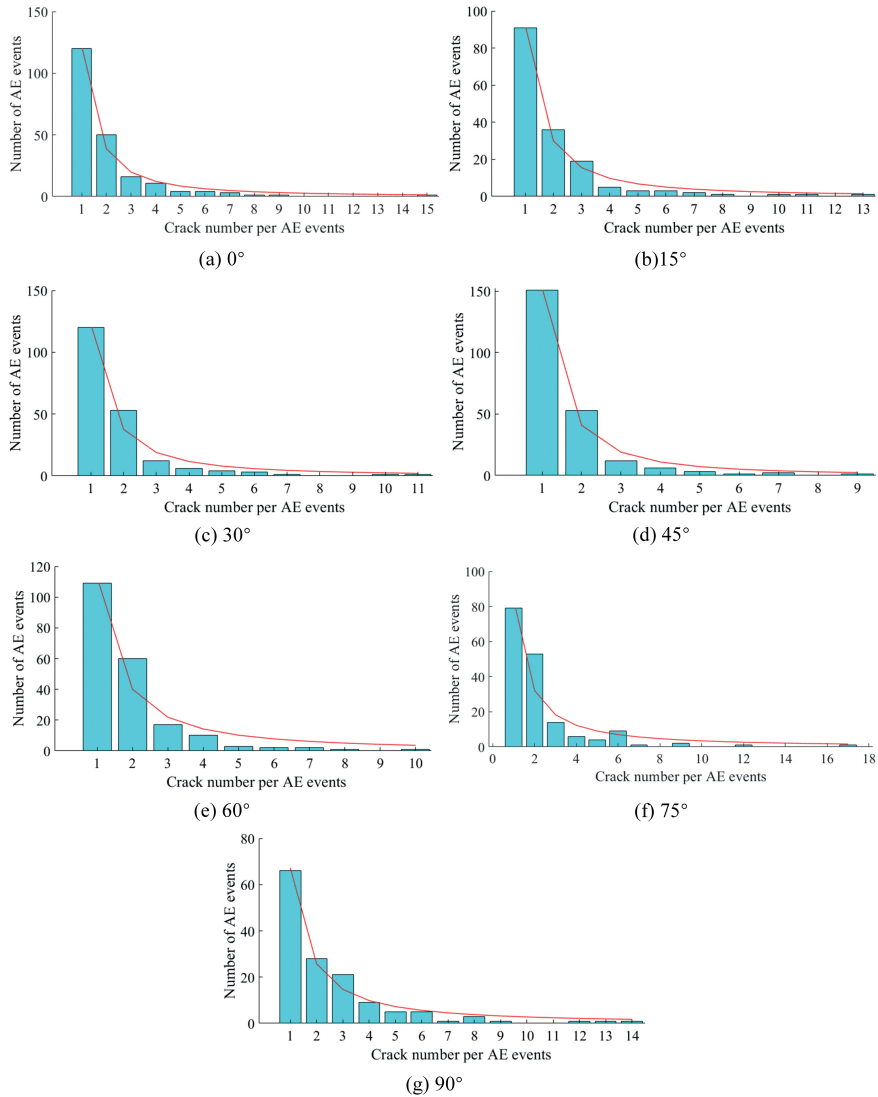


Fig. 14. Relationship between the number of AE events and the number of micro-cracks in each AE event

In addition, for the specimens with different pre-existing crack dip angles, the maximum number of micro-cracks contained in a single AE event also differs. For example, when the fracture dip angle is 75°, the maximum number of micro-fractures in a single AE event is 17, but there is only one such AE event. When the fracture dip angles are 45° and 60°, the number of micro-fractures in a single AE event is the lowest, 9 and 10, respectively, and there is only one of each event. This is consistent with the strength of samples under

different fracture dip angles shown in Fig. 4. There is a certain relationship between the number of micro-cracks in a single AE event and the strength of the specimen; much more data are needed to confirm and define this relationship.

4. Conclusions

To analyse the micro-mechanisms of crack initiation and propagation in pre-cracked rock mass under tensile loading, the focal mechanism of AE events during loading is simulated by the discrete element method. The temporal and spatial distributions of AE events during loading are analysed. At the same time, the relationship between the type of micro-cracks, the magnitude of AE events, the number of AE events and the number of micro-cracks is discussed. The main conclusions are as follows:

1. The macroscopic failure mode is affected by the angle of the pre-existing crack. When the dip angle $\beta \leq 60^\circ$, micro-cracks initiate at the pre-existing crack tip and expand to the loading end, resulting in macro failure. When the dip angle $\beta > 60^\circ$, micro-cracks initiate on the upper and lower surfaces of the pre-existing crack and expand to the loading end, rather than from the tip of the pre-existing crack.
2. For different pre-existing crack angles, at the crack initiation point, there are tensile micro-cracks, shear micro-cracks appear randomly in the loading process, and mixed micro-cracks mainly appear near the loading end. The results show that the micro-crack initiation of pre-cracked rock mass under radial compression is caused by tensile stress.
3. When rock undergoes ultimate failure, the number of tensile micro-cracks is significantly greater than that of shear micro-cracks and mixed micro-cracks, indicating that the macro failure mode of pre-existing crack samples in the process of radial compression is mainly controlled by tensile failure.
4. There is a power law relationship between the AE event magnitude and cumulative event frequency. There is a narrow distribution of events with the most frequent magnitude in samples with pre-existing crack dip angles of 45° and 60° . Laboratory tests show that the bearing capacity of the specimens is relatively low when the dip angles are 45° and 60° . This shows that the magnitude distribution can reflect the rock strength to a certain extent.
5. The relationship between the number of AE events and micro-cracks approximates a negative exponential function. Only one micro-fracture has the largest number of AE events, accounting for 50–60% of the total AE events, and the AE events with 10 or more micro-cracks account for only 1% of the total number of AE events. The maximum number of micro-cracks of a single AE in high strength samples is greater than that in low strength samples. There is a good correspondence between the maximum number of micro-cracks of a single AE and the peak strength.

In conclusion, the numerical simulation of acoustic emission simulation algorithm based on MT theory can better compensate for the shortcomings of laboratory technical means. As a reliable technology, in-depth micro mechanism research on pre cracked rock is conducive to the safe and stable operation of the rock project.

Acknowledgements

Financial supports for this work, provided by the Fundamental Research Funds for the Central Universities (2018ZDPY08, 2021GJZPY15) and the National Natural Science Foundation of China (41474122, 41974164, 51323004), are gratefully acknowledged.

References

- [1] D.Y. Li, L.N.Y. Wong, “The Brazilian Disc Test for Rock Mechanics Applications: Review and New Insights”, *Rock Mechanics and Rock Engineering*, 2013, vol. 46, no. 2, pp. 269–287, DOI: [10.1007/s00603-012-0257-7](https://doi.org/10.1007/s00603-012-0257-7).
- [2] S.H. Cho, Y. Ogata, K. Kaneko, “Strain-rate dependency of the dynamic tensile strength of rock”, *International Journal of Rock Mechanics and Mining Sciences*, 2003, vol. 40, no. 5, pp. 763–777, DOI: [10.1016/S1365-1609\(03\)00072-8](https://doi.org/10.1016/S1365-1609(03)00072-8).
- [3] L.X. Xiong, X.J. Zhang, Z.Y. Xu, et al., “Scale effect of cement mortar specimens subjected to high temperatures using uniaxial compressive and splitting tensile tests”, *Archives of Civil Engineering*, 2020, vol. 66, no. 3, pp. 139–155, DOI: [10.24425/ace.2020.134389](https://doi.org/10.24425/ace.2020.134389).
- [4] J. Claesson, B. Boholi, “Brazilian test: stress field and tensile strength of anisotropic rocks using an analytical solution”, *International Journal of Rock Mechanics and Mining Sciences*, 2002, vol. 39, no. 8, pp. 991–1004, DOI: [10.1016/S1365-1609\(02\)00099-0](https://doi.org/10.1016/S1365-1609(02)00099-0).
- [5] X. Chang, J. Tang, G.Z. Wang, et al., “Mechanical performances of rock-like disc containing circular inclusion subjected to diametral compression”, *Archives of Civil and Mechanical Engineering*, 2018, vol. 18, no. 2, pp. 356–370, DOI: [10.1016/j.acme.2017.07.008](https://doi.org/10.1016/j.acme.2017.07.008).
- [6] L.X. Xiong, H.Y. Yuan, Y. Zhang, et al., “Experimental and Numerical Study of the Uniaxial Compressive Stress-Strain Relationship of a Rock Mass with Two Parallel Joints”, *Archives of Civil Engineering*, 2019, vol. 65, no. 2, pp. 67–80, DOI: [10.2478/ace-2019-0019](https://doi.org/10.2478/ace-2019-0019).
- [7] E. Hoek, Z.T. Bieniawski, “Brittle fracture propagation in rock under compression”, *International Journal of Fracture*, 1965, vol. 1, no. 3, pp. 137–155, DOI: [10.1007/BF00186851](https://doi.org/10.1007/BF00186851).
- [8] Y. Fujii, Y. Ishijima, “Consideration of fracture growth initial fracture at the surface of from an inclined slit and inclined rock and mortar in compression”, *International Journal of Rock Mechanics and Mining Sciences*, 2004, vol. 41, no. 6, pp. 1035–1041, DOI: [10.1016/j.ijrmms.2004.04.001](https://doi.org/10.1016/j.ijrmms.2004.04.001).
- [9] S.Q. Yang, H.W. Jing, “Strength failure and crack coalescence behavior of brittle sandstone samples containing a single fissure under uniaxial compression”, *International Journal of Fracture*, 2011, vol. 168, no. 2, pp. 227–250, DOI: [10.1007/s10704-010-9576-4](https://doi.org/10.1007/s10704-010-9576-4).
- [10] T. Liu, B.Q. Lin, Q.L. Zou, et al., “Mechanical behaviors and failure processes of precracked specimens under uniaxial compression: A perspective from microscopic displacement patterns”, *Tectonophysics*, 2016, vol. 672, pp. 104–120, DOI: [10.1016/j.tecto.2016.01.027](https://doi.org/10.1016/j.tecto.2016.01.027).
- [11] Q.B. Lin, P. Cao, H. Wang, et al., “An Experimental Study on Cracking Behavior of Precracked Sandstone Specimens under Seepage Pressure”, *Advances in Civil Engineering*, 2018, vol. 2018, art. ID 4068918, DOI: [10.1155/2018/4068918](https://doi.org/10.1155/2018/4068918).
- [12] X. Chang, X. Zhang, L. Cheng, et al., “Crack path at bedding planes of cracked layered rocks”, *Journal of Structural Geology*, 2022, vol. 154, art. ID 104504, DOI: [10.1016/j.jsg.2021.104504](https://doi.org/10.1016/j.jsg.2021.104504).
- [13] H. Awaji, S. Sato, “Combined mode fracture toughness measurement by the disk test”, *Journal of Engineering Materials and Technology*, 1978, vol. 100, no. 2, pp. 175–182, DOI: [10.1115/1.3443468](https://doi.org/10.1115/1.3443468).
- [14] C. Atkinson, R.E. Smelser, J. Sanchez, “Combined mode fracture via the cracked brazilian disk tes”, *International Journal of Fracture*, 1982, vol. 18, no. 4, pp. 279–291, DOI: [10.1007/BF00015688](https://doi.org/10.1007/BF00015688).
- [15] L. Luo, X. Bi, et al., “Study on Fracture Initiation and Propagation in a Brazilian Disc with a Preexisting Crack by Digital Image Correlation Method”, *Advances in Materials Science and Engineering*, 2017, vol. 2017, art. ID 2493921, DOI: [10.1155/2017/2493921](https://doi.org/10.1155/2017/2493921).

- [16] J. Zhou, Y. J. Zeng, Y.T. Guo, et al., “Effect of natural filling fracture on the cracking process of shale Brazilian disc containing a central straight notched flaw”, *Journal of Petroleum Science and Engineering*, 2021, vol. 196, art. ID 107993, DOI: [10.1016/j.petrol.2020.107993](https://doi.org/10.1016/j.petrol.2020.107993).
- [17] N. Erarslan, D.J. Williams, “Mixed-Mode Fracturing of Rocks Under Static and Cyclic Loading”, *Rock Mechanics and Rock Engineering*, 2013, vol. 46, no. 5, pp. 1035–1052, DOI: [10.1007/s00603-012-0303-5](https://doi.org/10.1007/s00603-012-0303-5).
- [18] Y. Tang, G.B. Xu, Y. Yan, et al., “Thermal Cracking Analysis of Microbial Cemented Sand under Various Strains Based on the DEM”, *Advances in Materials Science and Engineering*, 2018, vol. 2018, art. ID 7528746, DOI: [10.1155/2018/7528746](https://doi.org/10.1155/2018/7528746).
- [19] A. Abolfazl, F.M. Mohammad, Y.B. Alireza, et al., “DEM simulation of confining pressure effects on crack opening displacement in hydraulic fracturing”, *International Journal of Mining Science and Technology*, 2016, vol. 26, no. 4, pp. 557–561, DOI: [10.1016/j.ijmst.2016.05.004](https://doi.org/10.1016/j.ijmst.2016.05.004).
- [20] M.P.J. Schöpfer, S. Abe, C. Childs, et al., “The impact of porosity and crack density on the elasticity, strength and friction of cohesive granular materials: Insights from DEM modelling”, *International Journal of Rock Mechanics and Mining Sciences*, 2009, vol. 46, no. 2, pp. 250–261, DOI: [10.1016/j.ijrmms.2008.03.009](https://doi.org/10.1016/j.ijrmms.2008.03.009).
- [21] M.M. Wu, R. Huang, J.F. Wang, “DEM simulations of cemented sands with a statistical representation of micro-bond parameters”, *Powder Technology*, 2021, vol. 379, pp. 96–107, DOI: [10.1016/j.powtec.2020.10.047](https://doi.org/10.1016/j.powtec.2020.10.047).
- [22] N. Casas, G. Mollon, A. Daouadji, “DEM Analyses of Cemented Granular Fault Gouges at the Onset of Seismic Sliding: Peak Strength, Development of Shear Zones and Kinematics”, *Pure and Applied Geophysics*, 2022, vol. 179, no. 2, pp. 679–707, DOI: [10.1007/s00024-021-02934-5](https://doi.org/10.1007/s00024-021-02934-5).
- [23] Q. Geng, F. He, Z.Y. Lu, et al., “Geometry evolution of mesoscopic mechanical structures during the rock fragmentation process induced by tunnel boring machine (TBM) cutters”, *Royal Society Open Science*, 2022, vol. 9, no. 1, art. ID 211630, DOI: [10.1098/rsos.211630](https://doi.org/10.1098/rsos.211630).
- [24] X.J. Hu, X.N. Gong, H.B. Hu, et al., “Cracking behavior and acoustic emission characteristics of heterogeneous granite with double pre-existing filled flaws and a circular hole under uniaxial compression: Insights from grain-based discrete element method modeling”, *Bulletin of Engineering Geology and the Environment*, 2022, vol. 81, no. 4, art. ID 162, DOI: [10.1007/s10064-022-02665-4](https://doi.org/10.1007/s10064-022-02665-4).
- [25] J.F. Hazzard, R.P. Young, “Moment tensors and micromechanical models”, *Tectonophysics*, 2002, vol. 365, no. 1-3, pp. 181–197, DOI: [10.1016/S0040-1951\(02\)00384-0](https://doi.org/10.1016/S0040-1951(02)00384-0).
- [26] D.O. Potyondy, P.A. Cundall, “A bonded-particle model for rock”, *International Journal of Rock Mechanics and Mining Sciences*, 2004, vol. 41, no. 8, pp. 1329–1364, DOI: [10.1016/j.ijrmms.2004.09.011](https://doi.org/10.1016/j.ijrmms.2004.09.011).
- [27] S.Q. Yang, Y.H. Huang, P.G. Ranjith, et al., “Discrete element modeling on the crack evolution behavior of brittle sandstone containing three fissures under uniaxial compression”, *Acta Mechanica Sinica*, 2015, vol. 31, no. 6, pp. 871–889, DOI: [10.1007/s10409-015-0444-3](https://doi.org/10.1007/s10409-015-0444-3).
- [28] D. Huang, T.T. Zhu, “Experimental and numerical study on the strength and hybrid fracture of sandstone under tension-shear stress”, *Engineering Fracture Mechanics*, 2018, vol. 200, pp. 387–400, DOI: [10.1016/j.engfracmech.2018.08.012](https://doi.org/10.1016/j.engfracmech.2018.08.012).
- [29] Y. Wang, F. Cui, “Energy evolution mechanism in process of Sandstone failure and energy strength criterion”, *Journal of Applied Geophysics*, 2018, vol. 154, pp. 21–28, DOI: [10.1016/j.jappgeo.2018.04.025](https://doi.org/10.1016/j.jappgeo.2018.04.025).
- [30] B. Feignier, R.P. Young, “Moment tensor inversion of induced microseismic events: Evidence of non-shear failures in the $-4 < M < -2$ moment magnitude range”, *Geophysical Research Letters*, 1992, vol. 19, no. 14, pp. 1503–1506, DOI: [10.1029/92gl01130](https://doi.org/10.1029/92gl01130).
- [31] Z. Zhou, S.X. Chen, Z.J. Dai, et al., “Study on strength softening law of Cenozoic red sandstone based on point load test”, *Rock and Soil Mechanics*, 2021, vol. 42, no. 11, pp. 2997–3007, DOI: [10.16285/j.rsm.2021.0300](https://doi.org/10.16285/j.rsm.2021.0300).
- [32] C.H. Chen, C.S. Chen, J.H. Wu, “Fracture toughness analysis on cracked ring disks of anisotropic rock”, *Rock Mechanics and Rock Engineering*, 2008, vol. 41, pp. 539–562, DOI: [10.1007/s00603-007-0152-9](https://doi.org/10.1007/s00603-007-0152-9).
- [33] H. Amrollahi, A. Baghbanan, H. Hashemolhosseini, “Measuring fracture toughness of crystalline marbles under modes I and II and mixed mode I–II loading conditions using CCNBD and HCCD specimens”, *International Journal of Rock Mechanics and Mining Sciences*, 2011, vol. 48, no. 7, pp. 1123–1134, DOI: [10.1016/j.ijrmms.2011.06.015](https://doi.org/10.1016/j.ijrmms.2011.06.015).

-
- [34] J.P. Liu, Y.H. Li, S.D. Xu, et al., “Moment tensor analysis of acoustic emission for cracking mechanisms in rock with a pre-cut circular hole under uniaxial compression”, *Engineering Fracture Mechanics*, 2015, vol. 135, pp. 206–218, DOI: [10.1016/j.engfracmech.2015.01.006](https://doi.org/10.1016/j.engfracmech.2015.01.006).
- [35] S.D. Xu, Y.H. Li, J.P. Liu, “Detection of cracking and damage mechanisms in brittle granites by moment tensor analysis of acoustic emission signals”, *Acoustical Physics*, 2017, vol. 63, no. 3, pp. 359–367, DOI: [10.1134/S1063771017030137](https://doi.org/10.1134/S1063771017030137).
- [36] V.B. Smirnov, T.I. Kartseva, A.V. Ponomarev, et al., “On the Relationship between the Omori and Gutenberg–Richter Parameters in Aftershock Sequences”, *Izvestiya Physics of the Solid Earth*, 2020, vol. 56, no. 5, pp. 605–622, DOI: [10.1134/S1069351320050110](https://doi.org/10.1134/S1069351320050110).
- [37] J.S. Kim, K.S. Lee, W.J. Cho, et al., “A Comparative Evaluation of Stress-Strain and Acoustic Emission Methods for Quantitative Damage Assessments of Brittle Rock”, *Rock Mechanics and Rock Engineering*, 2015, vol. 48, no. 2, pp. 495–508, DOI: [10.1007/s00603-014-0590-0](https://doi.org/10.1007/s00603-014-0590-0).
- [38] A. Ghazvinian, H.R. Nejati, V. Sarfarazi, et al., “Mixed mode crack propagation in low brittle rock-like materials”, *Arabian Journal of Geosciences*, 2013, vol. 6, no. 11, pp. 4435–4444, DOI: [10.1007/s12517-012-0681-8](https://doi.org/10.1007/s12517-012-0681-8).

Received: 03.02.2022, Revised: 29.04.2022